Journal of Inorganic Biochemistry 192 (2019) 72–81

Contents lists available at ScienceDirect

Journal of Inorganic Biochemistry

journal homepage: www.elsevier.com/locate/jinorgbio

An inorganic magnetic fluorescent nanoprobe with favorable biocompatibility for dual-modality bioimaging and drug delivery

Hongen Guo[a], Yixia Zhang[a], Wenting Liang[b], Feifei Tai[a], Qingchen Dong[a,*], Ruiping Zhang[c,*], Baofeng Yu[d,*], Wai-Yeung Wong[a,*]

[a] MOE Key Laboratory of Interface Science and Engineering in Advanced Materials, Research Center of Advanced Materials Science and Technology, Taiyuan University of Technology, No. 79 Yingze West Street, Taiyuan 030024, China
[b] Institute of Environmental Sciences and Department of Chemistry, Shanxi University, Taiyuan 030006, China
[c] Imaging Department of Affiliated Tumor Hospital of Shanxi Medical University, Imaging Department of Shanxi Provincial Cancer Hospital, Taiyuan 030001, China
[d] Department of Biochemistry and Molecular Biology, Shanxi Medical University, Taiyuan 030001, China

ARTICLE INFO

Keywords:
Magnetic fluorescent nanocomposites
Multifunctional
Biocompatibility
Dual-modality imaging
Drug delivery

ABSTRACT

In this work, we present the development of a high water soluble biological nanoprobe through the covalent bonding of β-CD onto the surface of iron oxide-gold nanoclusters (Fe_3O_4@Au@β-CD). Fe_3O_4@Au@SiO_2 NPs were also prepared for comparison. The maximum emission peak of magnetic fluorescent NPs red-shifted by 30 nm and the lifetime was also elongated to 5.21 μs after surface modified with β-CD. The relaxivities and in vitro magnetic resonance imaging ability of the resultant magnetic fluorescent NPs were also studied, indicating that Fe_3O_4@Au@β-CD NPs have the lowest r_2/r_1 ratio and could be a potential T_2 contrast agent for MR imaging. The MTT assay proved that, Fe_3O_4@Au@β-CD NPs are of excellent water solubility and biocompatibility. In vitro confocal fluorescence imaging was also performed, manifesting that Fe_3O_4@Au@β-CD NPs can be selectively uptaken by gastric cancer cells (MGC-803) and exhibit red fluorescence in the cells. The preliminary drug loading and releasing measurements demonstrate that it can also act as targeted drug delivery nanosystem. All these experimental results indicate that, Fe_3O_4@Au@β-CD NPs hold great application perspective in the diagnosis and therapy of gastric cancer cells as biological nanoprobes.

1. Introduction

Design and synthesis of multifunctional nanomaterials have received numerous attention due to their potential applications in cancer cell imaging and treatment [1–3]. As we know, imaging techniques are the most important and commonly used in clinical practice for cancer detection, such as magnetic resonance imaging (MRI), fluorescent imaging (FI), ultrasound imaging (UI), X-ray computed tomography (CT), etc. [4–8] However, each one of these technologies has its limitations in practical application due to their sensitivity, spatial resolution, and complexity [9]. Rational combination of two or more imaging techniques is an effective way to increase the accuracy of diagnosis of cancer. For instance, the multimodal MRI/FI nanoprobes have been widely explored and shown the outstanding advantage of simultaneously providing both high-resolution histological information and high-sensitivity functional imaging [10–12]. Moreover, to avoid the secondary damage to patient and improve the cure rate, it is very desirable to endow the therapy ability to targeting detection agent. Through the surface molecular engineering of nanoparticles (NPs), multi-functionalities can be achieved on a single NP, such as multimodal imaging ability for detection and treatment [13–15].

Superparamagnetic iron oxide (SPIO) is the most studied nanomaterials for exploration of theranostic agents through surface functionalization [16–18]. For example, by assembling with noble metals such as Ag and Au, Fe_3O_4 NPs can exhibit MR/FI dual-modal imaging ability [19,20]. Especially, the Au nanoclusters are very appealing due to their excellent photostability, large Stokes shift and environmental friendliness. Nevertheless, biocompatibility of this type of materials is unsatisfied and has limited their practical application due to their poor water solubility [21]. Thus, further modification is particularly needed to address this crucial issue. To keep in mind that it is very preferred to integrate the diagnosis and therapy abilities together, suitable modification material should be considered cautiously. It is well known that, cyclodextrins (CDs) can protect drugs from physical, chemical and enzymatic degradation, as well as solubilize hydrophobic drugs, which allow them to be widely used as drug-delivery agents [22–26].

* Corresponding authors.
E-mail addresses: dongqingchen@tyut.edu.cn (Q. Dong), zrp_7142@sxmu.edu.cn (R. Zhang), wai-yeung.wong@polyu.edu.hk (W.-Y. Wong).

https://doi.org/10.1016/j.jinorgbio.2018.12.002
Received 13 July 2018; Received in revised form 30 November 2018; Accepted 2 December 2018
Available online 10 December 2018

Therefore, CDs are likely to improve the hydrophilicity of the magnetic fluorescent NPs through covalent bond interaction.

In this report, we present the development of a high water soluble biological nanoprobe through the covalent bonding of β-CD onto the surface of iron oxide-gold nanoclusters (Fe_3O_4@Au@β-CD), which possesses excellent features such as red fluorescence, cytocompatible and superparamagnetic, etc. The relaxivities and in vitro magnetic resonance imaging ability of the resultant magnetic fluorescent NPs were studied, indicating that Fe_3O_4@Au@β-CD NPs have the lowest r_2/r_1 ratio and could be a potential T_2 contrast agent for MR imaging. In vitro confocal fluorescence imaging was also performed and demonstrated. This study aims to develop composite nanomaterial with high water solubility and biocompatibility as multifunctional nanoprobe for cancer diagnosis and treatment. Fe_3O_4@Au@SiO_2 NPs were also prepared for comparison.

2. Experimental

2.1. Materials

All the solvents and chemicals that were used in the synthetic route were of reagent grades. The following materials were purchased from Energy Chemical Co.: hydrogen tetrachloroaurate ($HAuCl_4{\cdot}4H_2O$), L (+)-cysteine (L-cys), Iron(III) acetylacetonate ($Fe(acac)_3$), 4-dimethylaminopyridine (DMAP), *N*,*N*′-dicyclohexylcarbodiimide (DCC), diphenyl ether, oleylamine and cetyltrimethyl ammonium bromide (CTAB). *N*-hexane, dimethyl sulfoxide (DMSO) and alcohol were purchased from Sinopharm Chemical Reagent Co., Ltd., China. Fetal bovine serum, phosphate buffer saline (PBS), 3-(4,5-dimethyl-2-thiazolyl)-2,5-diphenyl-2-*H*-tetrazolium bromide (MTT), paraformaldehyde and formazan were purchased from Nanjing micro-world biology technology Co. Ltd. The gastric mucosal and gastric cancer cells were available in the Cell Bank of Type Culture Collection of Chinese academy of sciences. All the reagents were used as received without further purification. Deionized water was used in all the experiments.

2.2. Synthesis of L-cys-AuNCs

L-cys-AuNCs were prepared through the reduction of $HAuCl_4{\cdot}4H_2O$ with L-cys. Briefly, $HAuCl_4{\cdot}4H_2O$ (0.50 mmol, 0.22 g) was added to 30 mL deionized water, followed by the addition of L-cys solution (0.06 g L-cys in 5 mL water). The mixture was stirred at 25 °C for 5 min, and then continuously stirred for 24 h at 70 °C. After reaction completed, there was white precipitate formed, which was filtered and dried to give rise to L-cys-AuNCs in white powder (0.11 g) [27].

2.3. Synthesis of Fe_3O_4-CTAB magnetic NPs

$Fe(acac)_3$ (3 mmol, 0.706 g) was dissolved in oleylamine (15 mL) and benzyl ether (15 mL) mixed solution and magnetically stirred under a flow of nitrogen. The mixture was dehydrated at 110 °C for 1 h, then quickly heated to 300 °C at a heating rate of 20 °C/min and allowed to react for another 1 h. The black-brown mixture was cooled to room temperature and extract with ethanol (40 mL) to precipitate out the crude Fe_3O_4 MNPs, which was collected by centrifugation (8000 rpm, 10 min). The black product was then purified by dissolving in hexane (35 mL) and reprecipitating by addition of ethanol (50 mL) for 3 times to give rise to pure Fe_3O_4 MNPs in black powder (0.15 g).

Fe_3O_4 MNPs were further functionalized by CTAB to change it from hydrophobic to hydrophilic. In a typical process, Fe_3O_4 MNPs (0.05 g) was added into 10 mL of CTAB solution (2.5 mg mL^{-1}). A subsequent ultrasonication (~30 min) led to the formation of a stable black emulsion, which was vigorously stirred at room temperature for 24 h. After centrifugation to remove the free surfactants, the precipitated hydrophilic Fe_3O_4-CTAB MNPs were re-dispersed in water to obtain a stable dispersion [28].

2.4. Synthesis of Fe_3O_4@Au NPs

The above hydrophilic Fe_3O_4-CTAB MNPs (0.09 g) and L-cys-AuNCs (0.11 g) were mixed in ultrapure water and sonicated for 5 mins to form gray emulsion, which was then allowed to react for 6 h under room temperature. Afterwards, the reaction solution was centrifuged (8000 rpm, 10 min). The precipitate was separated and dried to generate the target Fe_3O_4@Au NPs in deep-gray color (0.10 g) [29].

2.5. Synthesis of Fe_3O_4@Au@SiO_2 NPs

The Fe_3O_4@Au NPs (0.12 g) were dispersed into the mixed solution of ethanol (80 mL) and water (20 mL). Then 1 mL ammonia aqueous (28 wt%) was added and the mixture was allowed to react for 15 min under stirring. TEOS (3 mL) was then added to react for 6 h. Afterwards, the final product Fe_3O_4@Au@SiO_2 NPs were obtain by centrifugation, which were then purified with ethanol and water, respectively (0.61 g) [30].

2.6. Synthesis of Fe_3O_4@Au@β-CD NPs

The Fe_3O_4@Au NPs (0.12 g) and β-CD (0.24 g) were dispersed in ultrapure water and allowed to react for 30 min at room temperature under vigorously stirring. Then DMAP (12 mg) and DCC (12 mg) were added to react overnight. After reaction completed, the color of solution was changed from black to brown-yellow. Afterwards, the reaction solution was centrifuged (8000 rpm, 10 min). The precipitate was separated and dried to give rise to the target Fe_3O_4@Au@β-CD NPs in brown-yellow color (0.27 g, 67.5%) [31].

2.7. Characterization

Fourier transform infrared (FT-IR), Ultraviolet-visible (UV–vis) absorption and photoluminescence (PL) spectra were measured with Bruker Tensor 27 spectrometer, Hitachi U3900 spectrometer and Horiba FluoroMax-4 spectrofluorometer, respectively. FT-IR spectra were measured in the 500–4000 cm^{-1} region with samples dispersed in KBr pellets. Transmission electron microscopy (TEM) (JEM-2010F, USA) operated at an acceleration voltage of 200 kV was used to study the morphology and average diameter of the as-synthesized NPs. The average hydrodynamic diameter of solvated NPs was evaluated with Zetasizer Nano ZS90. Thermogravimetric analysis (TGA) curves were recorded to quantify the composition of samples under a nitrogen atmosphere with a heating rate of 10 °C/min using the NETZSCH TG 209 F3 Tarsus. The confocal microscopy images were obtained under a confocal fluorescence microscope (LSM-880, Zeiss) at 37 °C. The M-H curves were recorded on the LakeShore 7410 at room temperature, and the relaxivities were measured on a Smartracer relaxometer (all the samples were dissolved in water and measured at 37 °C under a magnetic field of 0.17 T).

2.8. Cell culture and MTT assay

The gastric mucosal and gastric cancer cells (210 cells per mL) were cultured in Dulbecco's modified Eagle's medium supplemented with 10% fetal bovine serum-1640 using a 96-well plate at 37 °C in a humidified incubator containing 5% CO_2. For the MTT cell viability assay, coverslips (15 mm) were placed in each well of a 24-well plate. GES-1 and MGC-803 cells were seeded at a density of 5×10^4 cells per well in 1 mL DMEM medium and grown for 24 h. Then, Fe_3O_4@Au, Fe_3O_4@Au@SiO_2, and Fe_3O_4@Au@β-CD NPs with various concentrations (25, 50, 100 and 200 μg mL^{-1}) were dispersed in DMEM solutions with new culture medium, and allowed to incubate for 2 h at 37 °C in the presence of 5% CO_2. After exposure, the supernatant was removed and cells were washed immediately with PBS. Then, an aliquot of 150 μL 10% fetal bovine serum-1640 and 20 μL MTT stock solution

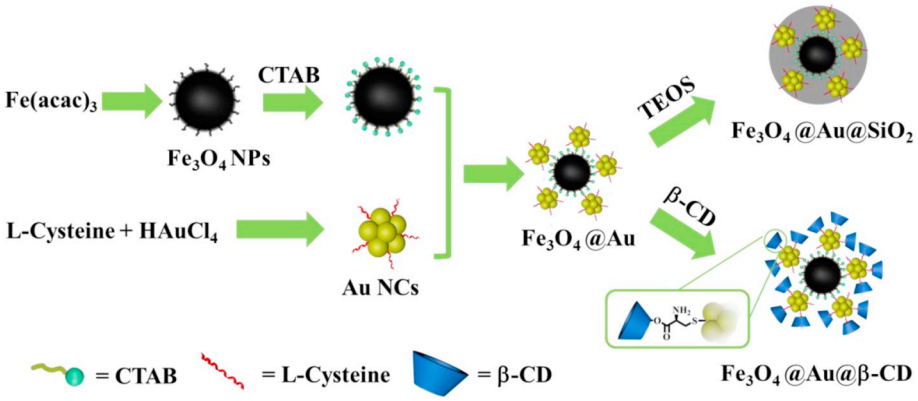

Scheme 1. Synthetic routes of Fe_3O_4@Au, Fe_3O_4@Au@SiO_2, Fe_3O_4@Au@β-CD NPs.

(5 mg mL^{-1} in PBS, pH 7.4) were subsequently added to each well and incubated for 4 h at 37 °C. Finally, an aliquot of 150 μL DMSO was added to dissolve the formazan crystals after removing the culture medium. The resulting mixture was shaken for 10 min at room temperature. The optical density (OD) of the mixture was measured at 490 nm using a standard micro plate reader (Scientific Multiskan MK3, thermo, USA), and the cell viability was expressed by the ratio of the OD of MTT in the experimental samples to that of the cells incubated with culture medium only according to the following formula [32]:

Cell viability = (OD value of the experimental group /OD value of the control group) × 100%.

2.9. Cell imaging

Coverslips (15 mm) were placed in each well of a 24-well plate. GES-1 and MGC-803 cells were seeded at a density of 5×10^4 cells per well in 1 mL DMEM medium with 10% fetal bovine serum (FBS) and grown for 24 h at 37 °C in the presence of 5% CO_2. Then, the old culture mediums were replaced by 1 mL of DMEM solutions containing Fe_3O_4@Au, Fe_3O_4@Au@SiO_2, and Fe_3O_4@Au@β-CD NPs (100 μg mL^{-1}), respectively. After incubation for 2 h at 37 °C in the presence of 5% CO_2, the cells in the culture medium were washed three times with PBS buffer solution (pH = 7.4) to remove the excess NPs in advance, and fixed with 4% (by mass) paraformaldehyde in PBS for 20 min at 37 °C. All the experiments were performed in triplicate to reduce the randomness of the experiments.

2.10. In vitro drug loading and release efficiency measurements

The maximum loading amount of DOX in Fe_3O_4@Au@β-CD NPs was evaluated by mixing 1 mg of Fe_3O_4@Au@β-CD NPs with 2 mL of 200 μg mL^{-1} DOX ethanol solution. After ultrasonic treatment for 120 min, the resulting suspension was centrifuged at 8000 rpm for 20 min. The residual DOX content of the supernatant at different time was collected and measured by UV–vis absorption spectroscopy at λ = 483 nm. The loading amount (LA) and loading efficiency (LE) can be calculated according to the formulas (1 and 2):

$$LA\% = (M_0 - M)/M_{NPs} \times 100\% \quad (1)$$

$$LE\% = (M_0 - M)/M_0 \times 100\% \quad (2)$$

where M_0 is the original DOX content in the corresponding loading solution, M is the remaining DOX content and M_{NPs} is the mass of Fe_3O_4@Au@β-CD NPs [33].

To study the drug release of DOX-loaded Fe_3O_4@Au@β-CD, 2.0 mg of DOX-loaded Fe_3O_4@Au@β-CD NPs were dispersed in 10 mL PBS with different pH values (5.0 and 7.4) and placed in dialysis bags (MWCO, 3500 Da). The dialysis bags were dipped in 30 mL of PBS at 37 °C with gently shaking in a water bath shaker under dark condition. 2 mL of supernatant solution was taken out periodically through centrifugation and an equal amount of fresh PBS was added at the same time to maintain the total solution volume constant at 10 mL. The release DOX was determined by fluorescence spectroscopy with excitation wavelength at 480 nm and emission wavelength at 550 nm. The cumulative DOX release can be calculated by the following formula (3):

$$\text{Drug release (\%)} = Mt/M0 \times 100\% \quad (3)$$

where M_t and M_0 are the amount of drug released at time t and that of drug initially loaded onto NPs, respectively [34].

3. Results and discussion

3.1. Synthesis and characterization

The synthetic routes of Fe_3O_4@Au, Fe_3O_4@Au@SiO_2, and Fe_3O_4@Au@β-CD NPs are shown in Scheme 1. Iron(III) acetylacetonate was chosen as the precursor to generate Fe_3O_4 NPs according to the procedure as reported in literature [28]. Au nanoclusters (AuNCs) were synthesized according to the similar method reported by Xie et al. with L-cys as reductant instead of GSH [27]. The Fe_3O_4 NPs were further modified by CTAB to be positive charging and hydrophilic. Then Fe_3O_4 NPs and AuNCs were assembled together through the electrostatic interaction to give rise to Fe_3O_4@Au NPs. Afterwards, Fe_3O_4@Au NPs were allowed to react with tetraethoxysilane (TEOS) by using ammonia as reducing agent to produce Fe_3O_4@Au@SiO_2 NPs. Finally, we use β-CD to modify Fe_3O_4@Au NPs through esterification, which gives rise to covalent linked Fe_3O_4@Au@β-CD NPs.

Fig. 1(a–f) exhibit the digital photos of Fe_3O_4@Au, Fe_3O_4@Au@SiO_2 and Fe_3O_4@Au@β-CD NPs at daylight and under UV lamp. It can be seen obviously that, Fe_3O_4@Au and Fe_3O_4@Au@SiO_2 are gray powder while Fe_3O_4@Au@β-CD NPs are brown, and all these NPs exhibited red fluorescence under UV irradiation. From Fig. 1(g, h) we can observe distinctly that, Fe_3O_4@Au, Fe_3O_4@Au@SiO_2 and Fe_3O_4@Au@β-CD were attracted onto the wall of the vial by an external magnet and also shown red emission. This suggests that all these NPs are magnetic. Fig. 1(i, k) are the saturated solutions of at daylight and under UV excitation, which implies that these NPs can also emit red fluorescence in solution.

To further investigate the composition and magnetic properties of the above NPs, we performed the measurements of FT-IR spectra and M-H curves as shown in Fig. 2. From the IR spectra of Fig. 2a, we can observe the characteristic absorption peaks caused by stretching vibration of Si—O—Si bonds. By comparing with the spectra of Fe_3O_4@Au NPs and β-CD, the characteristic absorption peaks of Fe_3O_4@Au@β-CD NPs with the wavenumbers of 3390 cm^{-1}, 1650 cm^{-1} and 1155 cm^{-1} correspond to the stretching vibration of —OH, —C(=O)— and C—O—C bonds, respectively. Moreover, the absorption peak located at

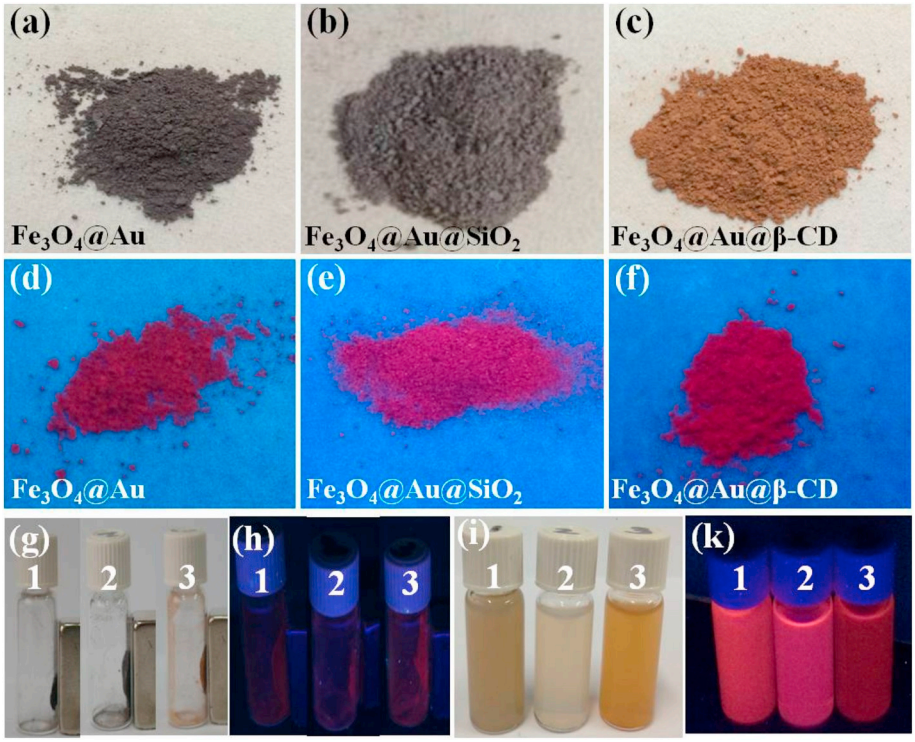

Fig. 1. Photos of (a, d) Fe_3O_4@Au NPs, (b, e) Fe_3O_4@Au@SiO_2 NPs, and (c, f) Fe_3O_4@Au@β-CD NPs at daylight and under UV lamp, respectively; (g, h) photos of Fe_3O_4@Au (**1**), Fe_3O_4@Au@SiO_2 (**2**) and Fe_3O_4@Au@β-CD (**3**) NPs absorbing by a magnet at daylight and under UV lamp; (i, k) photos of saturated solutions of Fe_3O_4@Au (**1**), Fe_3O_4@Au@SiO_2 (**2**) and Fe_3O_4@Au@β-CD (**3**) NPs at daylight and under UV lamp.

3390 cm^{-1} corresponding to the stretching vibration of −OH was enhanced significantly, manifesting that β-CD was successfully composited with Fe_3O_4@Au NPs. Thermogravimetric analysis was acquired to quantify the grafting amount of β-CD. Fig. S1 exhibits the TGA curves of Fe_3O_4@Au and Fe_3O_4@Au@β-CD NPs measured at the heating rate of 10 °C/min in nitrogen flow. The total weight losses for Fe_3O_4@Au and Fe_3O_4@Au@β-CD NPs were determined to be about 47% and 54%, respectively, indicating about 7% surface grafting amount of Fe_3O_4@Au by β-CD. For both TGA curves, a mass loss can be observed between 200 and 400 °C, which could be attributed to the degradation of organic moieties (i.e. CTAB, oleylamine, L-cysteine and β-CD) from the nanoparticle surface. Fig. 2b shows the M-H curves of Fe_3O_4@Au, Fe_3O_4@Au@SiO_2 and Fe_3O_4@Au@β-CD NPs, which imply that all these NPs are superparamagnetic. The saturated magnetization of Fe_3O_4@Au, Fe_3O_4@Au@SiO_2 and Fe_3O_4@Au@β-CD NPs are determined to be 7.76, 7.41, 2.83 emu g^{-1}, respectively. The low saturated magnetization of Fe_3O_4@Au@β-CD NPs should be attributed to their low crystallinity, which resulted from the aggregation of Fe_3O_4@Au NPs in the core [35].

3.2. Morphology study

Morphologies of the resulting Fe_3O_4@Au, Fe_3O_4@Au@SiO_2, and Fe_3O_4@Au@β-CD NPs were investigated by transmission electron microscopy (TEM), as shown in Fig. 3. It can be seen clearly from Fig. 3(a–c) that both the Fe_3O_4@Au and Fe_3O_4@Au@SiO_2 NPs exhibit spherical morphology, while the Fe_3O_4@Au@β-CD NPs hold a distinct core-shell structure. From the high resolution TEM (HRTEM) image of a Fe_3O_4@Au NP in Fig. 3d, we can observe the clear continuous fringe patterns with the interplanar distances of around 0.1124 nm and 0.1135 nm, which correspond to the (311) d-spacing of face-centered cubic (fcc) Au NPs (JCPDS no. 04-0784) and (642) d-spacing of fcc Fe_3O_4 NPs (JCPDS no. 26-1136). In Fig. 3e, the (311) d-spacing of fcc Au NPs, (642) and (444) d-spacings of fcc Fe_3O_4 NPs with the interplanar distances of 0.1127 nm (0.1130 nm), 0.1120 nm and 0.1206 nm, respectively, can also be seen clearly. The observation of fringe patterns in the TEM implies that these NPs are highly crystalline. Fig. 3f shows the HRTEM image of a Fe_3O_4@Au@β-CD NP, from which we can observe the clear core-shell structure with the shell thickness of 20 nm

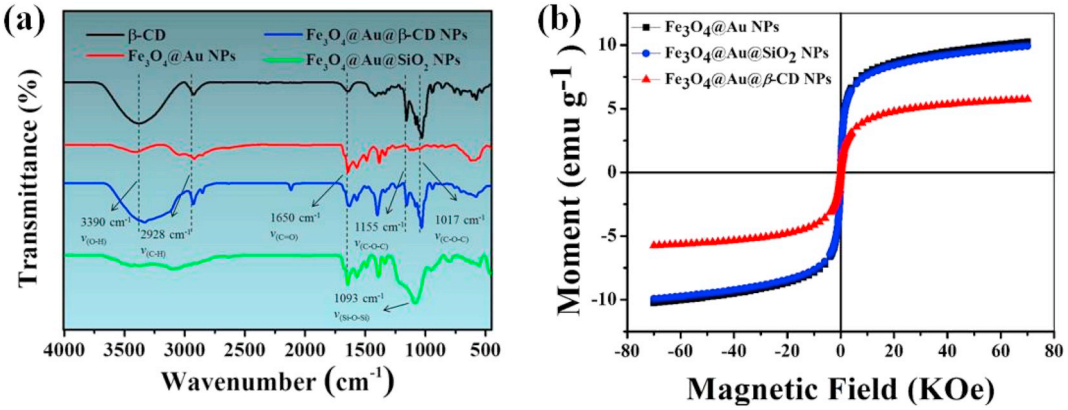

Fig. 2. (a) Infrared absorption spectra and (b) M-H curves of Fe_3O_4@Au, Fe_3O_4@Au@SiO_2, and Fe_3O_4@Au@β-CD NPs, respectively.

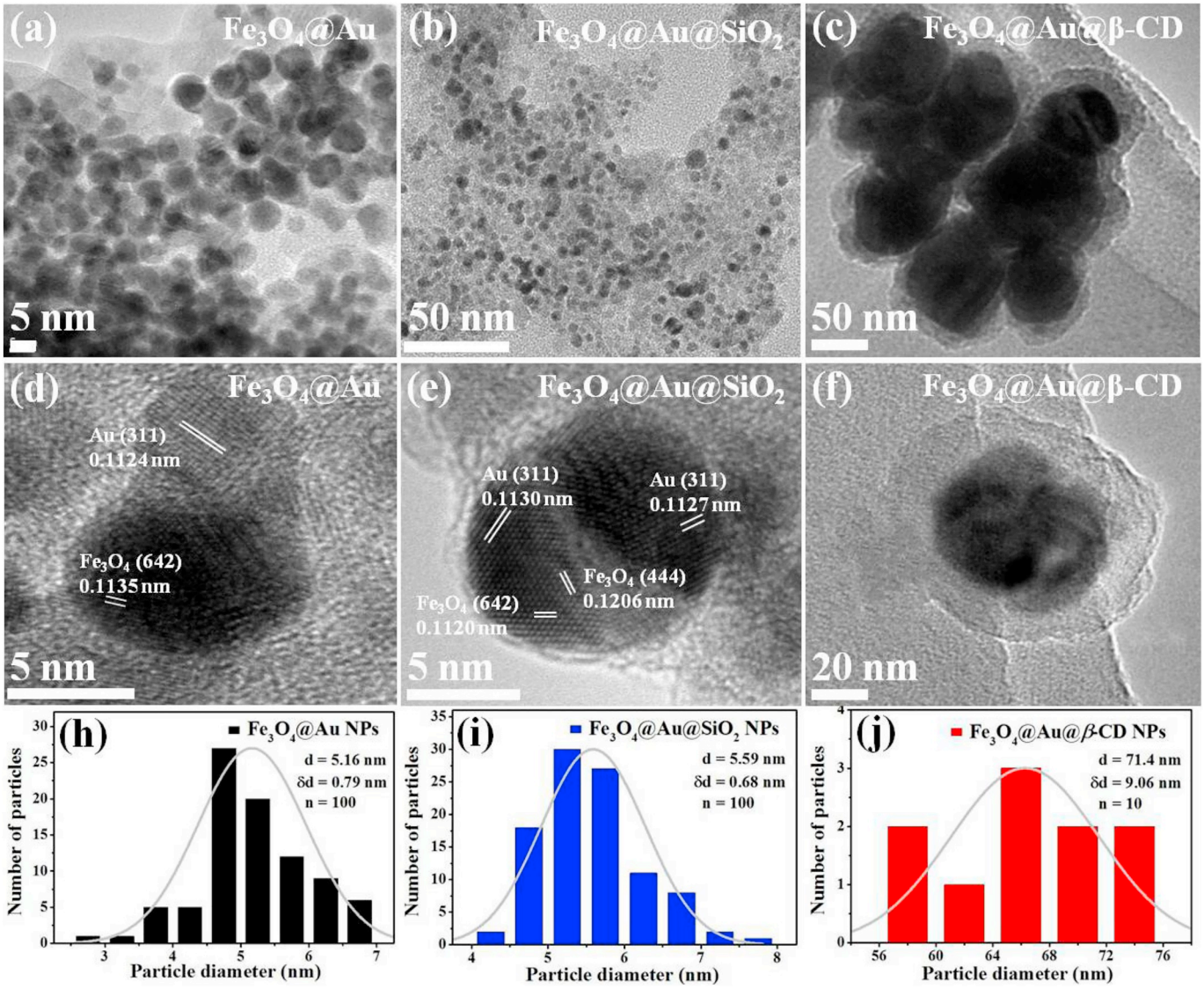

Fig. 3. TEM and HRTEM images of (a, d) Fe_3O_4@Au, (b, e) Fe_3O_4@Au@SiO_2 and (c, f) Fe_3O_4@Au@β-CD NPs; Size distribution of (h) Fe_3O_4@Au, (i) Fe_3O_4@Au@SiO_2 and (j) Fe_3O_4@Au@β-CD NPs.

around. The obvious core-shell structure of Fe_3O_4@Au@β-CD NPs might be formed due to the self-assembly effect of β-CD, which force the aggregation of Fe_3O_4@Au NPs in the core. Fig. 3(h–j) display the histogram of the size distribution of the TEM images (Fig. 3a–c), indicating that the as-synthesized Fe_3O_4@Au, Fe_3O_4@Au@SiO_2, and Fe_3O_4@Au@β-CD NPs have an effective average size of 5.16, 5.59 and 71.40 nm, respectively, as depicted in Fig. 3(h–j).

The hydrodynamic size of Fe_3O_4@Au@β-CD NPs dissolved in ultrapure water was measured to be 178.1 nm as determined by dynamic light scattering (DLS), which is much higher than that calculated from the TEM image. This could be attributed to the aggregation of Fe_3O_4@Au@β-CD NPs due to the solvation effect induced by hydrogen bond interactions of β-CD in solution [36]. Moreover, the average size of the resulting NPs increase significantly with increasing the reaction amount of β-CD as determined by the DLS measurement (see Figs. S2, S3 and Table S1), which further proved the existence of intermolecular hydrogen bond interaction of β-CD.

3.3. Photophysical properties

To investigate the intrinsic photophysical properties of Fe_3O_4@Au, Fe_3O_4@Au@SiO_2 and Fe_3O_4@Au@β-CD NPs, their UV–Vis absorption spectra, photoluminescence (PL) spectra (at room temperature both in water solution and in powder state) were measured and presented in Fig. 4. As shown in Fig. 4(a), Fe_3O_4@Au, Fe_3O_4@Au@SiO_2 and Fe_3O_4@Au@β-CD NPs exhibit two sets of absorption bands at 260 nm and 360 nm around in their UV–Vis absorption spectra. By comparing with Fe_3O_4@Au and Fe_3O_4@Au@SiO_2 NPs, the intensity of 360 nm absorption band of Fe_3O_4@Au@β-CD NPs increased clearly and the maximum absorption peak was red-shifted to 385 nm. This is consistent with the PL intensity increase in the range of 600–700 nm, as shown with the dashed line in Fig. 4(a). This might be ascribed to the larger particle size and aggregation-induced emission (AIE) effect caused by the compact arrangement of Fe_3O_4@Au in the core of Fe_3O_4@Au@β-CD NPs [37]. From the PL spectra of Fe_3O_4@Au, Fe_3O_4@Au@SiO_2 and Fe_3O_4@Au@β-CD NPs in powder states (Fig. 4b), we can see clearly that the maximum emission peak of Fe_3O_4@Au@β-CD NPs red shifted by 30 nm to 650 nm by comparing to Fe_3O_4@Au and Fe_3O_4@Au@SiO_2 NPs. Fig. 4(c) displays the overlay PL spectra of Fe_3O_4@Au@β-CD NPs at different concentrations in water, which demonstrates that the PL intensity grows significantly in the range of 600–700 nm with the increase of the concentration of Fe_3O_4@Au@β-CD NPs aqueous solution. Fig. S4 shows the absorption and emission spectra of Fe_3O_4@Au@β-CD NPs in aqueous solutions with different pH values and in PBS solution

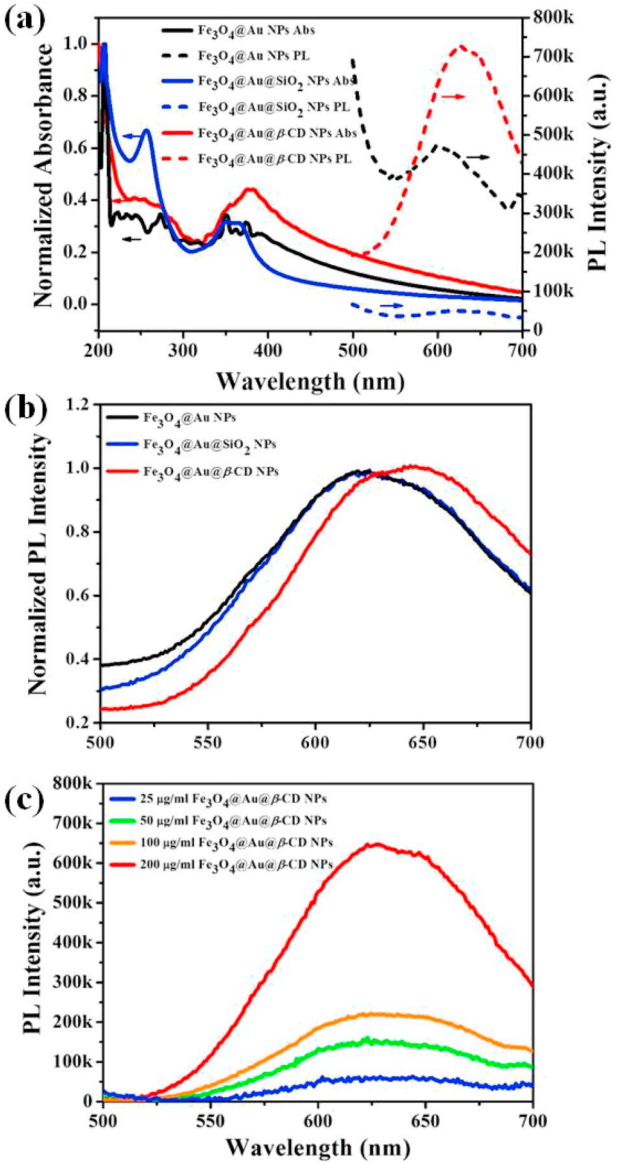

Fig. 4. (a) The Normalized overlay absorption and emission spectra (λ_{ex} = 365 nm) of Fe_3O_4@Au, Fe_3O_4@Au@SiO_2 and Fe_3O_4@Au@β-CD NPs with the same concentration (200 μg mL^{-1}) in water at 298 K; (b) Normalized PL spectra of Fe_3O_4@Au, Fe_3O_4@Au@SiO_2 and Fe_3O_4@Au@β-CD NPs in powder at 298 K (λ_{ex} = 365 nm); (c) PL spectra of Fe_3O_4@Au@β-CD NPs at different concentrations (25, 50, 100 and 200 μg mL^{-1}) in water at 298 K (λ_{ex} = 365 nm).

(100 μg mL^{-1}). It can be observed that, the absorption and emission wavelengths and intensities have no much change, manifesting the relatively high stability of NPs in solutions with different pH values or high ionic strength.

The lifetimes of Fe_3O_4@Au, Fe_3O_4@Au@SiO_2 and Fe_3O_4@Au@β-CD NPs were studied by time-resolved photoluminescence (TRPL) spectra (as shown in Fig. 5). The PL decay data is fitted through the formula (1), while the average excitons lifetime of NPs were determined by formula (2) [38]. The lifetimes of Fe_3O_4@Au, Fe_3O_4@Au@SiO_2 and Fe_3O_4@Au@β-CD NPs are finally calculated to be 4.68, 2.77 and 5.21 μs, respectively. Hence, the radiative transition rate of Fe_3O_4@Au NPs is increased significantly after surface modified by SiO_2 and decreased after modified with β-CD. And the longer average lifetime of Fe_3O_4@Au@β-CD NPs comparing with Fe_3O_4@Au and Fe_3O_4@Au@SiO_2 NPs could be attributed to its particular structure and composition, which is also favorable in the bioimaging of cancer cells.

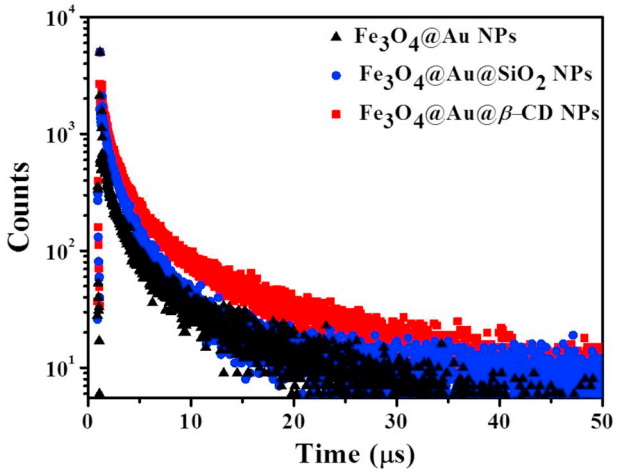

Fig. 5. Time-resolved PL spectra measured for Fe_3O_4@Au, Fe_3O_4@Au@SiO_2 and Fe_3O_4@Au@β-CD NPs in water at 298 K (λ_{ex} = 375 nm).

$$I_{PL}(t) = \sum_{i=1}^{n} A_i \exp\left(-\frac{t}{\tau_i}\right) \quad (4)$$

$$[\tau] = \frac{B_1\tau_1^2 + B_2\tau_2^2 + B_3\tau_3^2}{B_1\tau_1 + B_2\tau_2 + B_3\tau_3} \quad (5)$$

The luminescence quantum yield of Fe_3O_4@Au@β-CD NPs was determined as follows with Rhodamine 6G (Φ_F^{Std} = 0.95 in water) as the reference [39]:

$$\Phi_F = \Phi_F^{Std} \times \frac{FA^{Std}n^2}{F^{Std}A(n^{Std})^2} \quad (6)$$

where A and A^{Std} are the absorbances of the sample and the standard Rhodamine 6G, respectively. F and F^{Std} are the areas under the luminescence curves of the sample and the Rhodamine 6G, respectively. n and n^{Std} are the refractive indices of the solvent used for the sample and standard Rhodamine 6G, respectively. The quantum yield of Fe_3O_4@Au@β-CD NPs was finally calculated to be 0.6% in water.

3.4. Zeta-potential study

To study the zeta-potential change of NPs by introducing different surface modification layer, we measured the zeta-potential values of Fe_3O_4 NPs, Fe_3O_4-CTAB NPs, Fe_3O_4@Au NPs, Fe_3O_4@Au@β-CD NPs and L-cys-Au nanoclusters (NCs) dispersed in ultrapure water, which were measured to be −29.3 ± 1.3 mV, 40.1 ± 0.1 mV, 30.6 ± 0.2 mV, 12.8 ± 1.0 mV and −27.4 ± 1.0 mV, respectively (as displayed in Fig. 6). Therefore, after introducing CTAB, the zeta-potential of NPs can be dramatically changed from negative (−29.3 ± 1.3 mV) to positive (40.1 ± 0.1 mV) due to the positively charged trimethylammonium group. However, further modification with L-cys-Au nanoclusters (NCs) reduced the zeta-potential to 30.6 ± 0.2 mV, which can be understood easily by the negative zeta-potential of L-cys-Au NCs (−27.4 ± 1.0 mV). As it is well known, the zeta-potential of β-CD is negative [40]. Thus, the grafting of β-CD onto the surface of Fe_3O_4@Au NPs can further lower the zeta-potential to 12.8 ± 1.0 mV. Moreover, we studied the zeta potential of Fe_3O_4@Au@β-CD NPs with different grafting amount of β-CD. We can learn from Fig. S5 and Table S2 that the zeta potential decreased gradually with the increase of the grafting amount of β-CD, and turned from positive to negative when the reaction mass ratio is 1:6. The positive zeta-potential of as-synthesized Fe_3O_4@Au@β-CD NPs in this work (reaction mass ratio = 1:2) is favorable for the targeting of cancer cells due to the electrostatic interaction. In addition, the zeta-potential change of intermediates and final NPs can also prove the composition of

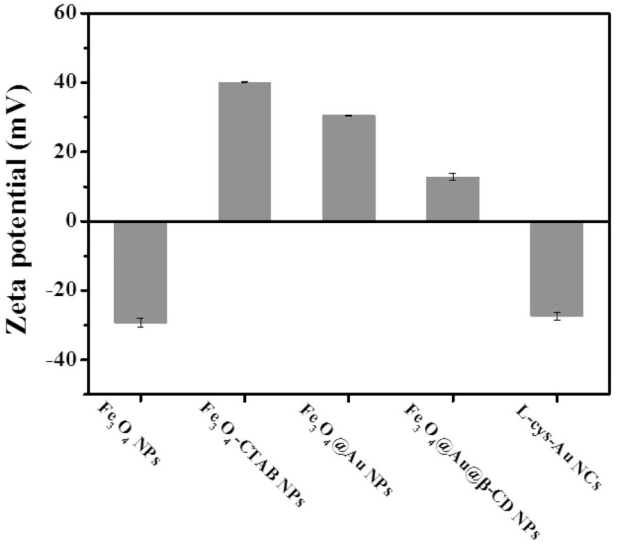

Fig. 6. Zeta-potential values of Fe_3O_4 NPs, Fe_3O_4-CTAB NPs, Fe_3O_4@Au NPs, Fe_3O_4@Au@β-CD NPs and L-cys-Au nanoclusters (NCs). Data are means ± SD.

Fe_3O_4@Au@β-CD NPs.

3.5. Biological application

3.5.1. MTT assay

The potential clinical applications of luminescent in the diagnosis of cancers or other diseases tend to depend on their water solubility and cytotoxicity. In this regard, we first investigate the solubility of as-synthesized Fe_3O_4@Au, Fe_3O_4@Au@SiO_2 and Fe_3O_4@Au@β-CD NPs. The as-prepared saturated aqueous solutions of Fe_3O_4@Au, Fe_3O_4@Au@SiO_2 and Fe_3O_4@Au@β-CD NPs were allowed to stew for 12 h. Afterwards, we observed that there were precipitate generated obviously in the saturated solution of Fe_3O_4@Au and Fe_3O_4@Au@SiO_2 NPs, while the Fe_3O_4@Au@β-CD one is still clear. Hence, after modification with β-CD, magnetic fluorescent NPs can be dispersed in water stably, which would be beneficial for its future application in biological system.

Then, we performed the MTT and apoptosis assay to evaluate the cytotoxicity of Fe_3O_4@Au, Fe_3O_4@Au@SiO_2 and Fe_3O_4@Au@β-CD NPs and viability of cells. As shown in Fig. 7, the viability of the gastric mucosal cells (GES-1) and gastric cancer cells (MGC-803) still remained close to 90% after incubation with Fe_3O_4@Au, Fe_3O_4@Au@SiO_2 and Fe_3O_4@Au@β-CD NPs for 24 h, respectively, even at the concentration of 200 μg mL^{-1}; these conditions are quite harsher than that used for cell incubation and imaging. The results demonstrate that all these NPs exhibit excellent biocompatibility to gastric mucosal and gastric cancer cells.

3.5.2. Magnetic relaxivity study

To explore the MRI imaging ability of Fe_3O_4@Au, Fe_3O_4@Au@SiO_2 and Fe_3O_4@Au@β-CD NPs, we performed measurement of the relaxivity of these materials with the content of [Fe] = 4 μM mL^{-1}. The relaxivity values (r_1 and r_2) are summarized in Table 1. As we can see clearly that, both r_1 and r_2 values of Fe_3O_4@Au@β-CD NPs are larger than Fe_3O_4@Au and Fe_3O_4@Au@SiO_2 NPs, while the r_2/r_1 ratio of Fe_3O_4@Au@β-CD NPs is lowest. To investigate the ability of Fe_3O_4@Au@β-CD NPs as MR contrast agents, samples of Fe_3O_4@Au@β-CD NPs were dissolved in water at different concentrations (0.01, 0.02, 0.04, 0.08 and 0.16 mM) and the T_2-weighted MR images were mapped by the 3.0 T MR scanner, as shown in Fig. 8a. It can be seen clearly that the image contrast decrease with the increase of concentration. The specific r_2 relaxivity was calculated from a linear regression curve fitting of $1/T_2$ (R_2, spin-spin relaxation rate) plotted against concentration in various aqueous solutions. As displayed in Fig. 8b, the r_2 value is determined to be 120.06 mM^{-1} s^{-1}, and the R_2 is enhanced with the increase of the concentration, manifesting that the NPs could serve as a T_2 contrast agent for MRI imaging [29,41].

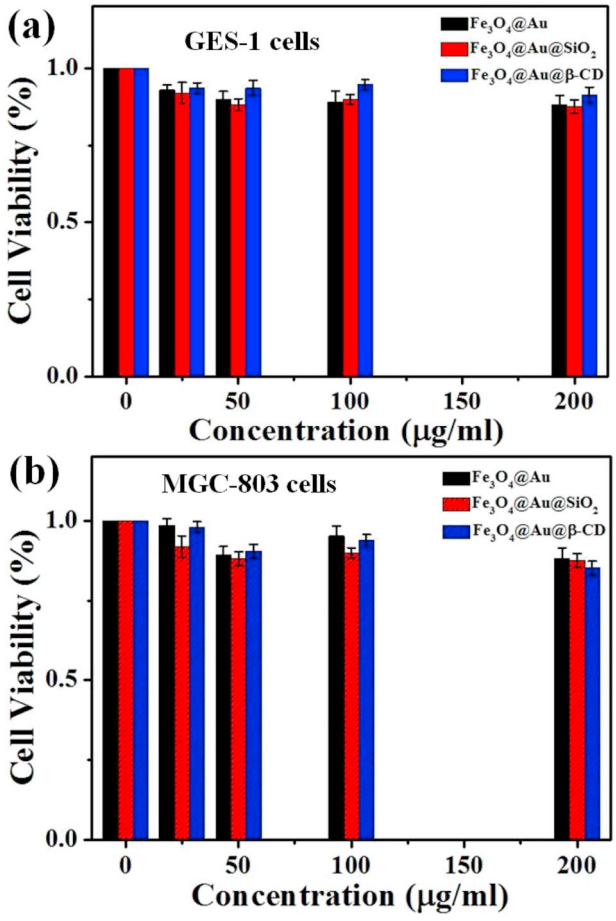

Fig. 7. MTT cell viability of (a) GES-1 cells and (b) MGC-803 cells incubated with Fe_3O_4@Au, Fe_3O_4@Au@SiO_2 and Fe_3O_4@Au@β-CD NPs at various concentrations.

Table 1
Relaxivities of as-synthesized Fe_3O_4@Au, Fe_3O_4@Au@SiO_2 and Fe_3O_4@Au@β-CD NPs.

Compound	r_1 (s^{-1} mM^{-1})	r_2 (s^{-1} mM^{-1})	r_2/r_1
Fe_3O_4@Au	1.2 ± 0.1	8.1 ± 0.2	6.8
Fe_3O_4@Au@SiO_2	2.0 ± 0.3	13.8 ± 1.7	6.9
Fe_3O_4@Au@β-CD	5.0 ± 0.9	26.3 ± 1.2	4.5

3.5.3. Cell imaging

The intracellular distribution of the Fe_3O_4@Au, Fe_3O_4@Au@SiO_2 and Fe_3O_4@Au@β-CD NPs in cells was evaluated by confocal laser scanning microscopy (CLSM), and the bright field, dark field and emerged images are shown in Fig. 9. Here, human gastric carcinoma MGC-803 cells and normal gastric epithelial cells (GES-1) were used for the imaging experiment, due to the high gastric cancer incidence in China, Japan, Eastern Europe and certain countries in Latin America [42]. From the bright field images, it can be observed clearly that GES-1 cells and MGC-803 cells incubated with these NPs still maintained their normal morphology, indicating the good biocompatibility of NPs at the tested doses and time. We can learn from the fluorescence dark field images collected at 610–680 nm (λ_{ex} = 405 nm) that, Fe_3O_4@Au NPs

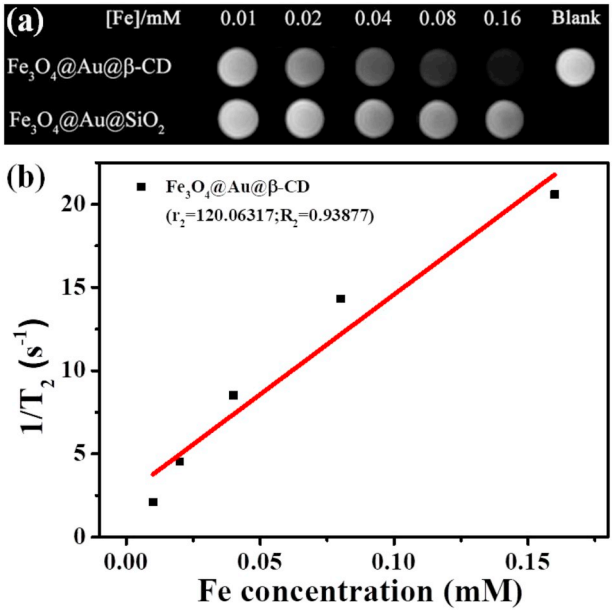

Fig. 8. (a) T_2-weighted MR images of Fe_3O_4@Au@β-CD NPs at various concentrations; (b) relaxation rate $1/T_2$ versus concentrations at room temperature using a 3.0 T MRI scanner.

are not able to be uptaken by MGC-803 cells due to its poor water solubility and biocompatibility, while Fe_3O_4@Au@β-CD NPs can be uptaken by MGC-803 cells and exhibit red fluorescence within the cells. And the fluorescence intensity enhanced significantly with the increase of concentration of Fe_3O_4@Au@β-CD NPs. However, Fe_3O_4@Au@β-CD NPs cannot be uptaken by GES-1 cells as shown in Fig. 9G, implying that Fe_3O_4@Au@β-CD NPs can selectively label MGC-803 cells. And this might be ascribed to the strong permeability of cancer cells. Although Fe_3O_4@Au@SiO_2 NPs can enter into the gastric cancer cells and exhibit red fluorescence, but the intensity is much lower than Fe_3O_4@Au@β-CD NPs.

To evaluate the targeted effectiveness of Fe_3O_4@Au@β-CD NPs, after incubation with Fe_3O_4@Au@β-CD NPs for 2 h and washing for several times with PBS solutions, the nucleuses of MGC-803 cells were further stained with 4′,6-diamidino-2-phenylindole (DAPI, 1.8 μM μL^{-1}) for 10 min. These dark field confocal images were collected in the range of 420–490 nm and 610–680 nm with wavelength of λ_{ex} = 405 nm, respectively. It can be seen clearly from the CLSM images in Fig. 10 that, the Fe_3O_4@Au@β-CD NPs could be uptaken by the nucleuses of MGC-803 cells instead of absorbing on the surface of cells. Therefore, the assembled nanocomposite Fe_3O_4@Au@β-CD could be used as functional probe for real-time cellular imaging [43].

3.5.4. *In vitro drug loading and release efficiency measurements*

To explore the drug delivery capability of the Fe_3O_4@Au@β-CD NPs, we first performed the DOX drug loading measurement. And the maximum loading amount of DOX in Fe_3O_4@Au@β-CD NPs was evaluated by mixing 1 mg of as-synthesized Fe_3O_4@Au@β-CD NPs with 2 mL of 200 μg mL^{-1} DOX ethanol solution. After ultrasonic treatment for 120 min, the resulting suspension was centrifuged at 8000 rpm for 20 min. The residual DOX content of the supernatant at different time was collected and measured by UV–vis absorption spectroscopy at λ = 483 nm (as shown in Fig. S6). It can be seen clearly that, the loading amount of DOX in Fe_3O_4@Au@β-CD NPs reached maximum with the absorption intensity of residual DOX in supernatant has no much change after 120 min. By measuring the absorption intensity, the maximum drug loading amount (LA) is 82 μg DOX per 1 mg of Fe_3O_4@Au@β-CD NPs, and the final LE% was determined to be 20.5%. Moreover, with increasing the amount of surface-grafted β-CD, the drug loading efficiency increased significantly from 15% (mass ratio of Fe_3O_4@A:β-CD = 1:0.5) to 25.5% (mass ratio of Fe_3O_4@Au:β-CD = 1:6) (as shown in Table S3).

Then, to quantitatively determine the release of DOX from the NPs, DOX loaded Fe_3O_4@Au@β-CD NPs were suspended in PBS at pH 7.4 (corresponding to the pH of blood) and PBS at pH 5.0 (corresponding to the pH of endosome) at 37 °C, respectively. The amount of released DOX at predetermined time points was measured by fluorescence spectroscopy with the excitation wavelength at 480 nm and emission

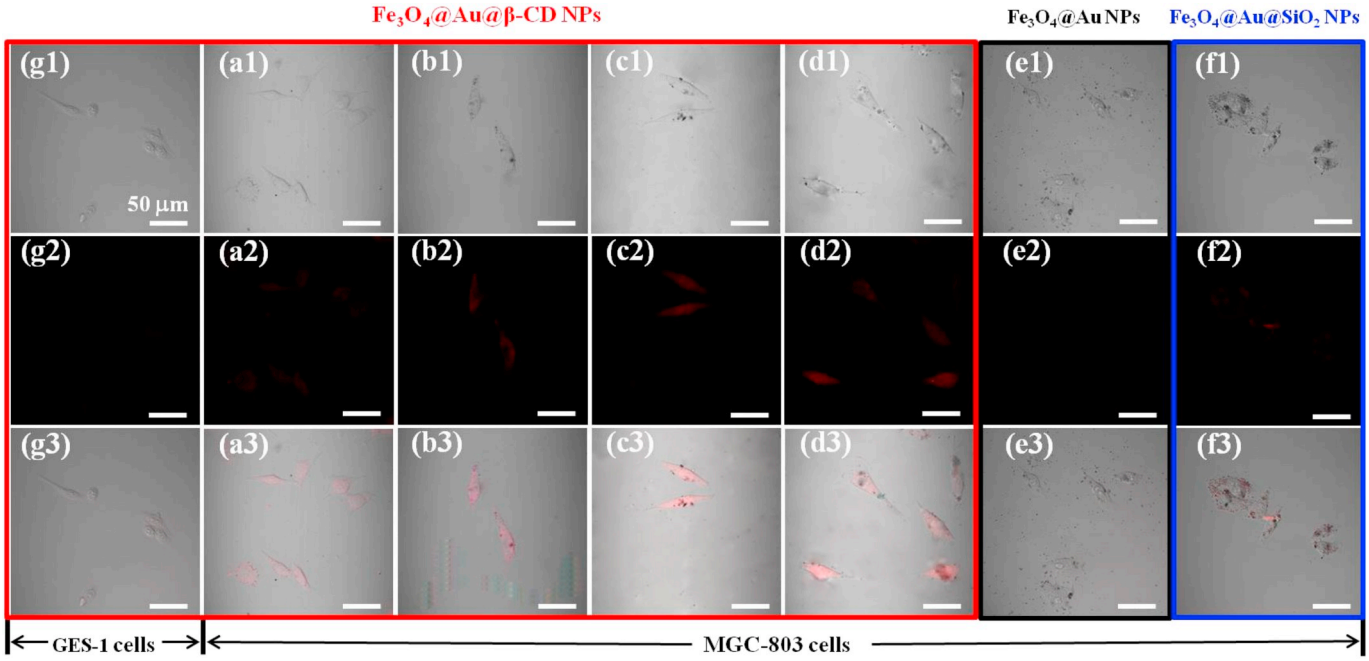

Fig. 9. Confocal images of MGC-803 cells incubated with (a–d) Fe_3O_4@Au@β-CD NPs at different concentrations (25, 50, 100 and 200 μg mL^{-1}), (e) Fe_3O_4@Au (100 μg mL^{-1}) and (f) Fe_3O_4@Au@SiO_2 (100 μg mL^{-1}); and (g) confocal images of GES-1 cells incubated with Fe_3O_4@Au@β-CD NPs (100 μg mL^{-1}) (collected at 610–680 nm, λ_{ex} = 405 nm).

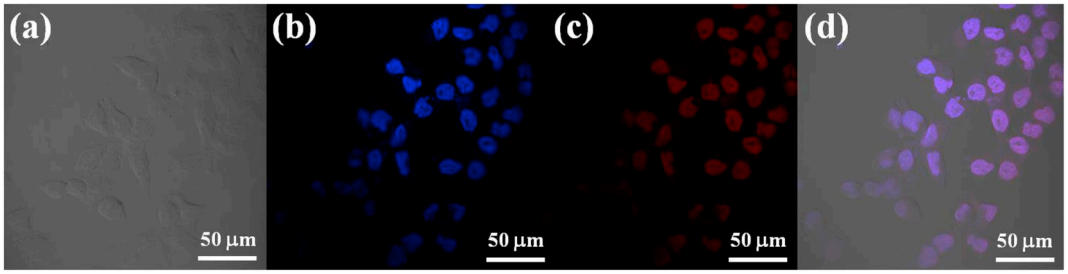

Fig. 10. Confocal images of MGC-803 cells after incubation with Fe_3O_4@Au@β-CD NPs at the concentration of 100 μg mL^{-1} (a) in light field, (b) in blue field, (c) in red field and (d) emerged. Cell nucleus was stained with DAPI (collected at 420–490 nm and 610–680 nm, λ_{ex} = 405 nm).

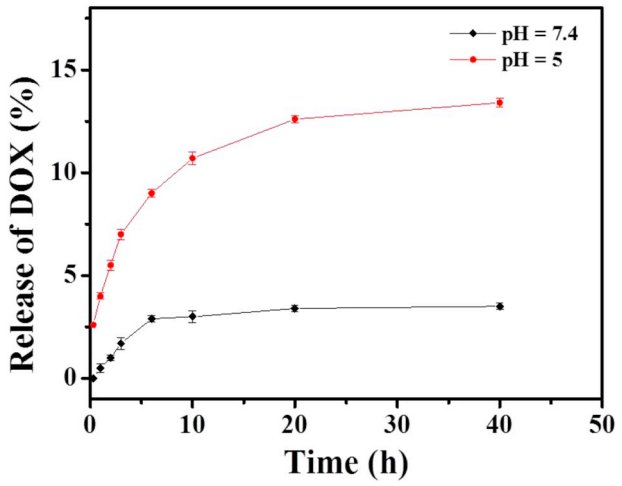

Fig. 11. In vitro drug releases of DOX-loaded Fe_3O_4@Au@β-CD NPs at pH 7.4 and 5.0, respectively.

wavelength at 550 nm. As shown in Fig. 11, the release of DOX loaded Fe_3O_4@Au@β-CD NPs is pH-sensitive. DOX release was faster and higher (13.4%) at pH 5.0 than that of 3.5% at pH 7.4 after 40 h incubation. This might be because that the weak interaction between DOX and β-CD is decreased under acidic environment which then facilitates the release of DOX from the central cavity of β-CD. Therefore, the as-synthesized Fe_3O_4@Au@β-CD NPs hold great biomedical application potential as a multifunctional nanoprobe.

4. Conclusions

To conclude, we used β-CD to surface modify magnetic fluorescent Fe_3O_4@Au NPs, and the water solubility and biocompatibility of resultant Fe_3O_4@Au@β-CD NPs enhanced significantly. Fe_3O_4@Au@SiO_2 NPs were also synthesized for comparison. The morphology, size distribution and photophysical properties of Fe_3O_4@Au, Fe_3O_4@Au@SiO_2 and Fe_3O_4@Au@β-CD NPs were fully investigated. Among them, Fe_3O_4@Au@β-CD NPs show uniform core-shell structure with average size of 50 nm. The maximum emission peak of magnetic fluorescent NPs red-shifted by 30 nm and the lifetime was also elongated to 5.21 μs after surface modified with β-CD. The biological experiments proved that, Fe_3O_4@Au@β-CD NPs are of excellent water solubility and biocompatibility; and it could serve as a T_2 contrast agents for MRI imaging. Moreover, the Fe_3O_4@Au@β-CD NPs can be selectively uptaken by gastric cancer cells (MGC-803) and exhibit red fluorescence in the cells. The preliminary drug loading and releasing measurements demonstrate that it can also act as targeted drug delivery nanosystem. All the above experimental results indicate that, the as-reported Fe_3O_4@Au@β-CD NPs in this work hold great application perspective in the diagnosis and therapy of gastric cancer cells as a multifunctional biological nanoprobe. Further investigation of these NPs in the application of in vivo and in vitro magnetic resonance imaging (MRI) and targeted drug delivery is in progress.

Abbreviations

$Fe(acac)_3$	acetylacetonate
AIE	aggregation-induced emission
AuNCs	Au nanoclusters
CTAB	cetyltrimethyl ammonium bromide
CT	computed tomography
CLSM	confocal laser scanning microscopy
CDs	cyclodextrins
DAPI	4′,6-diamidino-2-phenylindole
DMAP	4-dimethylaminopyridine
DMSO	dimethyl sulfoxide
MTT	3-(4,5-dimethyl-2-thiazolyl)-2,5-diphenyl-2-*H*-tetrazolium bromide
DLS	dynamic light scattering
FBS	fetal bovine serum
FI	fluorescent imaging
FT-IR	Fourier transform infrared
HRTEM	high resolution transmission electron microscopy
L-cys	L(+)-cysteine
LA	loading amount
LE	loading efficiency
MRI	magnetic resonance imaging
NCs	nanoclusters
NPs	nanoparticles
DCC	*N*,*N*′-dicyclohexylcarbodiimide
OD	optical density
PBS	phosphate buffer saline
PL	photoluminescence
SPIO	superparamagnetic iron oxide
TEOS	tetraethoxysilane
TGA	thermogravimetric analysis
TRPL	time-resolved photoluminescence
TEM	transmission electron microscopy
UI	ultrasound imaging
UV–vis	ultraviolet-visible

Acknowledgements

We acknowledge the financial support from the National Natural Science Foundation of China (Grant No.: 61774109, 81371628, 81571747, 81602506). This work was also supported by the Youth "Sanjin" Scholar Program, the Key R&D Project of Shanxi Province (International cooperation program, No. 201603D421032, 201703D421023), the Natural Science Foundation of Shanxi Province (Grant No.: 2015011113), Fund Program for the Scientific Activities of Selected Returned Overseas Professionals in Shanxi Province, Shanxi Scholarship Council of China (No. 2015057), R. Zhang also thanks the financial support from the Key Research and Development Project of

Shanxi Province (No. 2016021, 201703D321015-3), Science and Technology Innovation Team Project (No. 201705D131026), Scientific and Technological Achievements Transformation Project of Shanxi Province (No. 201704D131006), Startup Foundation for Doctors of Shanxi Provincial Cancer Hospital (No. 2017A01).

Appendix A. Supplementary data

Supplementary data to this article can be found online at https://doi.org/10.1016/j.jinorgbio.2018.12.002.

References

[1] B.M. De, P.S. Ghosh, V.M. Rotello, Applications of nanoparticles in biology, Adv. Mater. 20 (2008) 4225–4241.
[2] S. Wang, P. Huang, X. Chen, Hierarchical targeting strategy for enhanced tumor tissue accumulation/retention and cellular internalization, Adv. Mater. 28 (2016) 7340–7364.
[3] X. Gao, Y. Cui, R.M. Levenson, W.K. Chung, S. Nie, In vivo cancer targeting and imaging with semiconductor quantum dots, Nat. Biotechnol. 22 (2004) 969–976.
[4] H. Lee, T.H. Shin, J. Cheon, R. Weissleder, Recent developments in magnetic diagnostic systems, Chem. Rev. 115 (2015) 10690–10724.
[5] R. Kumar, T.Y. Ohulchanskyy, I. Roy, S.K. Gupta, C. Borek, M.E. Thompson, P.N. Pradad, Near-infrared phosphorescent polymeric nanomicelles: efficient optical probes for tumor imaging and detection, ACS Appl. Mater. Interfaces 1 (2009) 1474–1481.
[6] E.T. Ahrens, J.W.M. Bulte, Tracking immune cells in vivo using magnetic resonance imaging, Nat. Rev. Immunol. 13 (2013) 755–763.
[7] D.A. Anders, S. Bongarzone, R. Fortt, A.D. Gee, N.J. Long, Electrochemical [^{11}C]CO_2 to [^{11}C]CO conversion for PET imaging, Chem. Commun. 53 (2017) 2982–2985.
[8] J. Gallo, I.S. Alam, J. Jin, Y.J. Gu, W.T. Wong, N.J. Long, PET imaging with multimodal up conversion nanoparticles, Dalton Trans. 43 (2014) 5535–5545.
[9] S.J. Zhu, Q.N. Meng, L. Wang, J.H. Zhang, Y.B. Song, H. Jin, et al., Highly photoluminescent carbon dots for multicolor patterning, sensors, and bioimaging, Angew. Chem. Int. Ed. 52 (2013) 3953–3957.
[10] T.H. Shin, Y. Choi, S. Kim, J. Cheon, Recent advances in magnetic nanoparticle-based multi-modal imaging, Chem. Soc. Rev. 44 (2015) 4501–4516.
[11] H. Yang, Y.M. Zhuang, H. Hu, X.X. Du, C.X. Zhang, X.Y. Shi, et al., Silica-coated manganese oxide nanoparticles as a platform for targeted magnetic resonance and fluorescence imaging of cancer cells, Adv. Funct. Mater. 20 (2010) 1733–1741.
[12] D. Ding, G. Wang, J.Z. Liu, K. Li, K.Y. Pu, Y. Hu, et al., Hyperbranched conjugated polyelectrolyte for dual-modality fluorescence and magnetic resonance cancer imaging, Small 8 (2012) 3523–3530.
[13] H. Chen, W. Zhang, G. Zhu, J. Xie, X. Chen, Rethinking cancer nanotheranostics, Nat. Rev. Mater. 2 (2017) (17024-1-18).
[14] J. Gao, H. Gu, B. Xu, Multifunctional magnetic nanoparticles: design, synthesis, and biomedical applications, Acc. Chem. Res. 42 (2009) 1097–1107.
[15] P. Zrazhevskiy, M. Sena, X. Gao, Designing multifunctional quantum dots for bioimaging, detection, and drug delivery, Chem. Soc. Rev. 39 (2010) 4326–4354.
[16] N. Lee, D. Yoo, D. Ling, M.H. Cho, T. Hyeon, J. Cheon, Iron oxide based nanoparticles for multimodal imaging and magnetoresponsive therapy, Chem. Rev. 115 (2015) 10637–10689.
[17] K. Ulbrich, K. Holá, V. Šubr, A. Bakandritsos, J. Tuček, R. Zbořil, Targeted drug delivery with polymers and magnetic nanoparticles: covalent and noncovalent approaches, release control, and clinical studies, Chem. Rev. 116 (2016) 5338–5431.
[18] J. Bao, W. Chen, T. Liu, Y. Zhu, P. Jin, L. Wang, et al., Bifunctional Au-Fe_3O_4 nanoparticles for protein separation, ACS Nano 1 (2007) 293–298.
[19] J. Song, B. Wu, Z. Zhou, G. Zhu, Y. Liu, Z. Yang, et al., Double-layered plasmonic-magnetic vesicles by self-assembly of Janus amphiphilic gold-iron(II,III) oxide nanoparticles, Angew. Chem. Int. Ed. 56 (2017) 8110–8226.
[20] Q. Ding, D.F. Liu, D.W. Guo, F. Yang, X.Y. Pang, R.C. Che, et al., Shape-controlled fabrication of magnetite silver hybrid nanoparticles with high performance magnetic hyperthermia, Biomaterials 124 (2017) 35–46.
[21] N.S. Abadeer, C.J. Murphy, Recent progress in cancer thermal therapy using gold nanoparticles, J. Phys. Chem. C 120 (2016) 4691–4716.
[22] M.X. Zhao, H.F. Huang, Q. Xia, L.N. Ji, Z.W. Mao, γ-Cyclodextrin–folate complex-functionalized quantum dots for tumor-targeting and site-specific labeling, J. Mater. Chem. 21 (2011) 10290–10297.
[23] H. Fu, Y.H. Zhou, W.L. Chen, Z.G. Deqing, M.L. Tong, L.N. Ji, et al., Complexation, structure, and superoxide dismutase activity of the imidazolate-bridged dinuclear copper moiety with β-cyclodextrin and its guanidinium-containing derivative, J. Am. Chem. Soc. 128 (2006) 4924–4925.
[24] C. Park, H. Youn, H. Kim, T. Noh, Y.H. Kook, E.T. Oh, et al., Cyclodextrin-covered gold nanoparticles for targeted delivery of an anti-cancer drug, J. Mater. Chem. 19 (2009) 2310–2315.
[25] S. Li, X. Wu, Q. Zhang, P. Li, Synergetic dual recognition and separation of the fungicide carbendazim by using magnetic nanoparticles carrying a molecularly imprinted polymer and immobilized β-cyclodextrin, Microchim. Acta 183 (2016) 1433–1439.
[26] Y. Wu, F. Zuo, Y. Lin, Z. Zheng, X. Ding, Fe_3O_4@Au nanoparticle modified by cyclodextrin, Polym. Mater. Sci. Eng. 30 (2014) 172–176.
[27] S.M. Wang, X.P. Song, Preparation of novel fluorescent Au nanoparticles and its application for Cu(2+) assay, J. Anhui Agric. Univ. 40 (2013) 155–158.
[28] Z. Xu, C. Shen, Y. Hou, H. Gao, S. Sun, Oleylamine as both reducing agent and stabilizer in a facile synthesis of magnetite nanoparticles, Chem. Mater. 21 (2009) 1778–1780.
[29] C. Wang, Y. Yao, Q. Song, Gold nanoclusters decorated with magnetic iron oxide nanoparticles for potential multimodal optical/magnetic resonance imaging, J. Mater. Chem. C 3 (2015) 5910–5917.
[30] Y.F. Huang, Z.L. Zhang, K.B. Kang, M. Zhao, T. Wen, Y.X. Liu, et al., Mitigation of metal-mediated losses by coating Au nanoparticles with dielectric layer in plasmonic solar cells, RSC Adv. 3 (2013) 16080–16088.
[31] L.Y. Jiang, L. Chen, Y.H. Zhang, Improved synthesis of 2-(acetyloxy)benzoic acid3-(nitrooxymethyl)phenyl ester, Chin. J. Med. Chem. 14 (2004) 178–179.
[32] Q. Zhang, T. Yin, G. Gao, J.G. Shapter, W. Lai, P. Huang, et al., Multifunctional core@shell magnetic nanoprobes for enhancing targeted magnetic resonance imaging and fluorescent labeling in vitro and in vivo, ACS Appl. Mater. Interfaces 9 (2017) 17777–17785.
[33] J. Gu, S. Su, M. Zhu, Y. Li, W. Zhao, Y. Duan, et al., Targeted doxorubicin delivery to liver cancer cells by PEGylated mesoporous silica nanoparticles with a pH-dependent release profile, Microporous Mesoporous Mater. 161 (2012) 160–167.
[34] M. Pooresmaeila, H. Namazia, β–Cyclodextrin grafted magnetic graphene oxide applicable as cancer drug delivery agent: synthesis and characterization, Mater. Chem. Phys. 218 (2018) 62–69.
[35] Q.C. Dong, W.S. Qu, W.Q. Liang, F.F. Tai, K.P. Guo, C.W. Leung, W.Y. Wong, Porphyrin-based metallopolymers: synthesis, characterization and pyrolytic study for the generation of magnetic metal nanoparticles, J. Mater. Chem. C 4 (2016) 5010–5018.
[36] W. She, K. Luo, C. Zhang, G. Wang, Y. Geng, L. Li, et al., The potential of self-assembled, pH-responsive nanoparticles of mPEGylated peptide dendron-doxorubicin conjugated for cancer therapy, Biomaterials 34 (2013) 1613–1623.
[37] Z. Luo, X. Yuan, Y. Yu, Q. Zhang, D.T. Leong, J.Y. Lee, et al., From aggregation-induced emission of Au(I)-thiolate complexes to ultrabright Au(0)@Au(I)-thiolate core-shell nanoclusters, J. Am. Chem. Soc. 134 (2012) 16662–16670.
[38] Q.C. Dong, F.F. Tai, H. Lian, B. Zhao, Z. Zhong, Z. Chen, et al., Realization of efficient light out-coupling in organic light-emitting diodes with surface carbon-coated magnetic alloy nanoparticles, Nanoscale 9 (2017) 2875–28820.
[39] O.J. Achadu, I. Uddin, T. Nyokong, The interaction between graphene quantum dots grafted with polyethyleneimine and Au@Ag nanoparticles: application as a fluorescence “turn-on” nanoprobe, J. Photochem. Photobiol. A 324 (2016) 96–105.
[40] P.K. Shende, R.S. Gaud, R. Bakal, D. Patil, Effect of inclusion complexation of meloxicam with β–cyclodextrin- and β–cyclodextrin-based nanosponges on solubility, in vitro release and stability studies, Colloids Surf. B: Biointerfaces 136 (2015) 105–110.
[41] L. Zhang, X. Zhong, L. Wang, H. Chen, Y.A. Wang, J. Yeh, et al., T1-weighted ultrashort echo time method for positive contrast imaging of magnetic nanoparticles and cancer cells bound with the targeted nanoparticles, J. Magn. Reson. Imaging 33 (2011) 194–202.
[42] L. Chen, C.C. Bao, H. Yang, D. Li, C. Lei, T. Wang, et al., A prototype of giant magnetoimpedance-based biosensing system for targeted detection of gastric cancer cells, Biosens. Bioelectron. 26 (2011) 3246–3253.
[43] C. Wang, Y. Wang, L. Xu, D. Zhang, M.X. Liu, X.W. Li, et al., Facile aqueous-phase synthesis of biocompatible and fluorescent Ag_2S nanoclusters for bioimaging: tunable photoluminescence from red to near infrared, Small 8 (2012) 3137–3142.